The Astronomical Journal, 164:101 (9pp), 2022 September https://doi.org/10.3847/1538-3881/ac80bf

The GAPS Programme at TNG XXXIX. Multiple Molecular Species in the Atmosphere of the Warm Giant Planet WASP-80 b Unveiled at High Resolution with GIANO-B*

Ilaria Carleo[1,20,21], Paolo Giacobbe[2], Gloria Guilluy[2,3], Patricio E. Cubillos[2,4], Aldo S. Bonomo[2], Alessandro Sozzetti[2], Matteo Brogi[2,5,6], Siddharth Gandhi[5,6,7], Luca Fossati[4], Diego Turrini[2], Katia Biazzo[8], Francesco Borsa[9], Antonino F. Lanza[8], Luca Malavolta[1,10], Antonio Maggio[11], Luigi Mancini[2,12,13], Giusi Micela[11], Lorenzo Pino[14], Ennio Poretti[15], Monica Rainer[9], Gaetano Scandariato[8], Eugenio Schisano[16], Gloria Andreuzzi[15,17], Andrea Bignamini[18], Rosario Cosentino[15], Aldo Fiorenzano[15], Avet Harutyunyan[15], Emilio Molinari[19], Marco Pedani[15], Seth Redfield[20], and Hristo Stoev[15]

[1] INAF—Osservatorio Astronomico di Padova, Vicolo dell'Osservatorio 5, I-35122 Padova, Italy; ilariacarleo.astro@gmail.com
[2] INAF—Osservatorio Astrofisico di Torino, Via Osservatorio, 20, I-10025 Pino Torinese To, Italy
[3] Observatoire Astronomique de l'Université de Genève, Chemin Pegasi 51b, 1290, Versoix, Switzerland
[4] Space Research Institute, Austrian Academy of Sciences, Schmiedlstraβe 6, Graz A-8042, Austria
[5] Department of Physics, University of Warwick, CV4 7AL, Coventry, UK
[6] Centre for Exoplanets and Habitability, University of Warwick, CV4 7AL, Coventry, UK
[7] Leiden Observatory, Leiden University, Postbus 9513, 2300 RA Leiden, The Netherlands
[8] INAF—Osservatorio Astrofisico di Catania, Via S. Sofia 78, I-95123 Catania, Italy
[9] INAF—Osservatorio Astronomico di Brera, Via E. Bianchi 46, I-23807 Merate, Italy
[10] Dipartimento di Fisica e Astronomia Galileo Galilei,Universitá di Padova, Vicolo dellOsservatorio 3, I-35122 Padova, Italy
[11] INAF—Osservatorio Astronomico di Palermo, Piazza del Parlamento, 1, I-90134 Palermo, Italy
[12] Department of Physics,University of Rome "Tor Vergata", Via della Ricerca Scientifica 1, I-00133 Rome, Italy
[13] Max Planck Institute for Astronomy, Königstuhl 17, D-69117—Heidelberg, Germany
[14] INAF—Osservatorio Astrofisico di Arcetri, Largo Enrico Fermi 5, I-50125 Firenze, Italy
[15] Fundación Galileo Galilei-INAF, Rambla José Ana Fernandez Pérez 7, E-38712 Breña Baja, TF, Spain
[16] Institute for Space Astrophysics and Planetology INAF-IAPS, Via Fosso del Cavaliere 100, I-00133 Rome, Italy
[17] INAF—Osservatorio Astronomico di Roma, Via Frascati 33, I-00078 Monte Porzio Catone, Italy
[18] INAF—Osservatorio Astronomico di Trieste, Via Tiepolo 11, I-34143 Trieste, Italy
[19] INAF Osservatorio Astronomico di Cagliari & REM, Via della Scienza, 5, I-09047 Selargius CA, Italy
[20] Astronomy Department and Van Vleck Observatory, Wesleyan University, Middletown, CT 06459, USA
[21] Instituto de Astrofísica de Canarias, Vía Láctea, 38205 La Laguna, Spain
Received 2022 May 3; revised 2022 June 25; accepted 2022 July 11; published 2022 August 18

Abstract

Detections of molecules in the atmosphere of gas giant exoplanets allow us to investigate the physico-chemical properties of the atmospheres. Their inferred chemical composition is used as tracer of planet formation and evolution mechanisms. Currently, an increasing number of detections is showing a possible rich chemistry of the hotter gaseous planets, but whether this extends to cooler giants is still unknown. We observed four transits of WASP-80 b, a warm transiting giant planet orbiting a late-K dwarf star with the near-infrared GIANO-B spectrograph installed at the Telescopio Nazionale Galileo and performed high-resolution transmission spectroscopy analysis. We report the detection of several molecular species in its atmosphere. Combining the four nights and comparing our transmission spectrum to planetary atmosphere models containing the signature of individual molecules within the cross-correlation framework, we find the presence of H_2O, CH_4, NH_3, and HCN with high significance, tentative detection of CO_2, and inconclusive results for C_2H_2 and CO. A qualitative interpretation of these results, using physically motivated models, suggests an atmosphere consistent with solar composition and the presence of disequilibrium chemistry and we therefore recommend the inclusion of the latter in future modeling of sub-1000 K planets.

Unified Astronomy Thesaurus concepts: Exoplanet atmospheres (487); Exoplanet astronomy (486); Exoplanet atmospheric composition (2021); Exoplanet detection methods (489); Transit photometry (1709); High resolution spectroscopy (2096); Molecular spectroscopy (2095)

1. Introduction

More and more studies of the atmospheres of hot and warm Jupiters, i.e., gaseous giant planets with equilibrium temperatures of $T_{\rm eq} \gtrsim 1000$ K and $T_{\rm eq} \lesssim 1000$ K, respectively, are yielding important advances in our understanding of the properties of exoplanetary atmospheres and of their possible links to planet formation and migration mechanisms (e.g., Madhusudhan 2019). These hot and warm giant planets are the ideal targets for atmospheric studies through the transmission spectroscopy technique, which allows us to probe the presence of atomic and molecular species at the atmospheric terminator

* Based on observations made with the Italian Telescopio Nazionale Galileo (TNG) operated by the Fundación Galileo Galilei (FGG) of the Istituto Nazionale di Astrofisica (INAF) at the Observatorio del Roque de los Muchachos (La Palma, Canary Islands, Spain).

during planetary transits. Indeed, the amplitude of spectral features in transmission spectroscopy is $\propto R_P H/R_\star^2$, where R_P and $R_\star$ are the planet and stellar radii, and $H = k_b T_{eq}/\mu\, g$ is the atmospheric scale height, with k_b the Boltzmann's constant, μ the mean molecular weight and g the planet surface gravity. Planets with higher T_{eq} and lower g and μ (hydrogen- and helium-dominated atmospheres) are thus the most favorable for atmospheric studies.

To date most of the insight from the atmospheres of transiting exoplanets comes from low-resolution ($R \sim 200$–2000) spectroscopy (LRS), especially from space thanks to HST, both in the optical and the near-InfraRed (nIR) wavelength ranges (e.g., Sing et al. 2016; Mansfield et al. 2021). High-resolution ($R \gtrsim 30{,}000$) spectroscopy (HRS), resolving the molecular absorption bands into thousands of individual lines, has also been proving an effective tool in the investigation of exoplanetary atmospheres (see, e.g., Birkby 2018 for a review), providing additional/complementary information to the low-resolution data. Indeed, while LRS is sensitive to broadband absorption features and the level of the spectral continuum relative to the stellar one (which gives information on the overall transit depth of the planet), HRS is sensitive to the core of the lines, and gives information on the line shape, line Doppler-shift, line-to-line and line-to-continuum contrast. This allows us to investigate higher layers (lower pressures) of the atmospheres, thus possibly studying layers lying above possible aerosol layers (Gandhi et al. 2020; Hood et al. 2020).

While past nIR HRS observations of warm and hot transiting giant exoplanets have detected at most two species, Giacobbe et al. (2021) have recently reported the detection of multiple molecules in the atmosphere of HD209458b, revealing a rich chemistry in this hot Jupiter and a carbon-to-oxygen ratio (C/O) close to or greater than 1, under the assumption of chemical equilibrium. This estimate of C/O would imply that the planet formed beyond the water condensation front (snowline) at about 2–3 au, and then migrated inward without substantial accretion of oxygen-rich solids or gas. Whether the rich chemistry found in the atmosphere of HD209458b pertains to other hot giant planets and the less studied warm Jupiters is unknown.

WASP-80 b is a transiting warm giant planet ($T_{eq} = 817$ K) that orbits a relatively active cool (late-K) dwarf every 3.07 days (Triaud et al. 2013). It has a radius of 0.952 R_J and a mass of 0.54 M_J (Triaud et al. 2013; Mancini et al. 2014; Bonomo et al. 2017; the system parameters are listed in Table 1). The resulting low density of $\sim$0.8 g cm^{-3} and the large transit depth of $\sim$3% make it a very good candidate for transmission spectroscopy.

Transmission spectroscopy with different data sets and ground-based instruments points to contrasting results. In fact, while Mancini et al. (2014) could not infer from their multicolor photometry analysis of WASP-80 b any variation in the planetary radius with wavelength due to large errors in the data, Kirk et al. (2018) found their transmission spectrum best represented by a Rayleigh scattering slope, which indicated the presence of hazes. Moreover, Sedaghati et al. (2017) claimed a detection of the pressure-broadened K I doublet, suggesting a clear and low-metallicity atmosphere for WASP-80 b, while Parviainen et al. (2018) found the opposite result, showing a flat transmission spectrum, with no significant K I and Na I absorptions. Most recently, Fossati et al. (2022) did not find any He planetary absorption, possibly indicating a low He abundance in the atmosphere of WASP-80 b. From the space-based HST/WFC3 data, Tsiaras et al. (2018) found no significant presence of water in the atmosphere of WASP-80 b. Also, Fisher & Heng (2018) performed a retrieval analysis on the HST/WFC3 data of WASP-80 b: although the best-fit model is the gray-cloud model with the water feature (see Figure 22 in Fisher & Heng 2018), the Bayesian statistics does not favor this model over a flat line, meaning no conclusive retrieved atmospheric properties can be reported.

Table 1
Parameters of the WASP-80 System

Parameter	Value	Reference
M_*	$0.570 \pm 0.050\ M_\odot$	Triaud et al. (2013)
R_*	$0.571 \pm 0.016\ R_\odot$	Triaud et al. (2013)
T_{eff}	4150 ± 100 K	Triaud et al. (2013)
[Fe/H]	-0.14 ± 0.16 dex	Triaud et al. (2013)
$v \sin i$	3.55 ± 0.33 km s^{-1}	Triaud et al. (2013)
logg$_*$	$4.689^{+0.012}_{-0.013}$ (cgs)	Triaud et al. (2013)
logR$'_{HK}$	-4.04 ± 0.02	Fossati et al. (2022)
P_{orb}	$3.06785234^{+0.00000083}_{-0.00000079}$ days	Triaud et al. (2015)
M_P	$0.540^{+0.035}_{-0.036}\ M_J$	Bonomo et al. (2017)
R_P	$0.952^{+0.026}_{-0.027}\ R_J$	Triaud et al. (2013)
K_P	122 ± 4 km s^{-1}	This work
T_{eq}	817 ± 20 K	This work[a]
ρ_P	$0.776^{+0.088}_{-0.078}$ g cm^3	Bonomo et al. (2017)
a	$0.03427^{+0.00096}_{-0.00100}$ au	Bonomo et al. (2017)
e	<0.020	Bonomo et al. (2017)

Note.
[a] We calculate the equilibrium temperature using the Equation (1) in López-Morales & Seager (2007), which assumes the Bond albedo equal to zero and redistribution factor f = 1/4.

In this letter, we present the analysis of the transmission spectrum of WASP-80 b using the HR GIANO-B data and the same technique as in Giacobbe et al. (2021). The observations and data reduction are described in Section 2, the resulting detections of molecules are presented in Section 3, which contains the central findings of this work. While this letter is mainly focused on the detection of multiple species, we give possible qualitative interpretations in Section 4 and, finally, the conclusions are given in Section 5.

2. Observations and Data Reduction

We observed four transits of WASP-80 b on 2019 August 09, 2019 September 21, 2020 June 26, and 2020 September 17 in GIARPS mode (Claudi et al. 2017), using GIANO-B (Oliva et al. 2006; Carleo et al. 2018) and HARPS-N (Cosentino et al. 2012, 2014) simultaneously, at the Telescopio Nazionale Galileo (TNG). While Fossati et al. 2022 presented an analysis of the optical portion of these observations together with a search for He I, in this work we mainly exploit the nIR GIANO-B data, in order to search for molecules in the atmosphere of this planet. These observations are part of the GAPS2[22] programme, aimed at exploring the diversity of planetary systems via the detection of planets around young stars (e.g., Carleo et al. 2020; Damasso et al. 2020), the search for inner small planetary companions to outer long-period giants (e.g., Barbato et al. 2020), and the observation and

[22] https://theglobalarchitectureofplanetarysystems.wordpress.com/

Table 2
Summary of the Results for Each Molecule for Both Cross-correlation and Likelihood Frameworks

Molecule	Database	Cross Correlation			Likelihood				Detection Status		
		v_{rest} (km s^{-1})	K_P (km s^{-1})	Significance (σ)	v_{rest} (km s^{-1})	K_P (km s^{-1})	Significance (σ)	log S	CC	LH	
H_2O	Exomol	0.0	123.0 ± 43.5	7.52	0.0	116^{+15}_{-14}	9.94	0.1	✓	✓	Detected
CH_4	HITEMP	−3.0	$115.5^{+64.5}_{-61.5}$	4.17	−1.0	124^{+34}_{-38}	4.08	0.1	✓	✓	Detected
NH_3	Exomol	0.0	$121.5^{+45.0}_{-55.5}$	4.96	0.0	119 ± 18	7.63	0.1	✓	✓	Detected
C_2H_2	Exomol	0.0	$129.0^{+70.5}_{-61.5}$	3.39[a]	−69.0	15^{+48}_{-15}	3.88	0.1	∼	×	Inconclusive
HCN	Exomol	0.0	$142.5^{+57.0}_{-55.5}$	4.11	0.0	134 ± 30	4.30	−0.5	✓	✓	Detected
CO	HITEMP	−3.0	$124.5^{+93.0}_{-64.5}$	4.62	−3.0	74^{+25}_{-24}	6.33[b]	0.3	✓	×	Inconclusive
CO_2 (4n)[c]	Ames	3.0	$199.5^{+163.5}_{-8.5}$	4.45	2.0	64^{+18}_{-16}	8.50[d]	0.2	×	×	Tentative
CO_2 (3n)[e]	Ames	0.0	126 ± 68.5	4.01	−1.0	147^{+18}_{-19}	7.09	0.2	✓	✓	

Notes. References for each molecule: H_2O (Polyansky et al. 2018), CH_4 (Hargreaves et al. 2020), NH_3 (Coles et al. 2019), C_2H_2 (Chubb et al. 2020), HCN (Harris et al. 2006; Barber et al. 2014), CO (Li et al. 2015), CO_2 (Huang et al. 2013, 2017).
[a] The most significant peak in the CC map is at $v_{rest} = 63$ km s^{-1} with a $\sigma = 3.65$ (see Figure 1).
[b] Peak is at an inconsistent KP.
[c] Four nights.
[d] Peak is at an inconsistent KP.
[e] Third night (2020 June 26) not included.

characterization of planetary atmospheres (e.g., Borsa et al. 2019; Guilluy et al. 2020; Pino et al. 2020; Giacobbe et al. 2021; Guilluy et al. 2022). GIANO-B covers a wavelength range of 0.95–2.45 μm split in fifty orders with a resolving power of $R \sim 50{,}000$. The spectra were reduced with the offline GOFIO pipeline (Rainer et al. 2018). The first three nights present a median signal-to-noise ratio (S/N) of ∼30 (with a maximum of ∼60), whereas the forth night is characterized by a median S/N ∼ 20 and a max S/N of ∼40 (see Fossati et al. 2022 for more details on the observations, observing log, and data reduction).

3. Transmission Spectroscopy and Search for Molecules

Cross-correlation analysis—for the transmission spectroscopy analysis, we followed the recipe by Giacobbe et al. (2021). Briefly, (a) we wavelength calibrated and aligned all the spectra to the observer's rest frame by using the Earth's absorption lines (telluric) as reference; (b) we removed the quasistationary (in wavelength) spectral components—not only tellurics but also the star at first order—using our custom principal component analysis approach; (c) we performed an optimal selection of the spectral orders, for each molecule and for each night, to discard the orders that do not contain enough signal (molecular lines) and/or are strongly contaminated by telluric and stellar lines; (d) we applied the cross-correlation (CC) technique between the observed data and the atmospheric models (described below) to investigate the presence of H_2O, CH_4, HCN, NH_3, CO, CO_2, C_2H_2. The cross-correlation function (CCF) is computed over a range of radial velocities between −252 and 252 km s^{-1} in steps of 3 km s^{-1} and for each molecule, spectral order, night, and exposure, and then coadded over all selected orders and nights. Even if we know with relative precision the theoretical planet's orbit radial velocity semiamplitude $K_P = 122 \pm 4$ km s^{-1}, we explore a range of K_P values between 0 and 200 km s^{-1} with steps of 3 km s^{-1}, in order to explore spurious detections near the expected K_P and to account for the uncertainty on K_P, as well as for dynamical effects of atmospheric winds. The resolution of 3 km s^{-1} was chosen to be equal to the half width half maximum of the instrumental profile for $R = 50{,}000$.

For each molecule we generated atmospheric transmission spectra using isothermal pressure/temperature (P/T) profiles using GENESIS (Gandhi & Madhusudhan 2017; Giacobbe et al. 2021). The choice of isothermal P/T profiles is guided by the fact that in transmission spectroscopy a change in temperature acts to change the planet scale height with altitude, leading in a change on the overall strength of the spectral lines. Thus, changing the shape of the P/T profile from isothermal to a more complex profile would not significantly change the chemistry in the atmosphere and the molecular detections.

The models span a range of pressure-temperature profiles ([100, 10^{-8}] bar, [−200, 200] K around T_{eq}) and volume mixing ratios (VMR; [10^{-12}, 10^{-1}]) for each species and are calculated at a constant wavenumber spacing of 0.01 cm^{-1} in the 0.9–2.6 μm wavelength range. We then convolved the spectra to the instrumental resolution of GIANO assuming a Gaussian profile with a FWHM ∼ 5.4 km s^{-1}, which corresponds to a spectral resolving power of $R \sim 50{,}000$. We adopted the latest and most suitable line lists for high-resolution spectroscopy (Gandhi et al. 2020), with CH_4 and CO from the HITEMP database (Rothman et al. 2010), H_2O, NH_3, HCN, and C_2H_2 from ExoMol (Tennyson et al. 2016), and CO_2 from Ames (Huang et al. 2013, 2017); see Table 2 for a full list of references for each molecular line list. These are broadened by the pressure and temperature into a Voigt profile according to their H_2 and He pressure-broadening coefficients. We additionally include collision-induced absorption from H_2–H_2 to H_2–He interactions (Richard et al. 2012) as a source of continuum opacity.

Since the CC is marginally dependent on VMR (Gandhi et al. 2020) when considering single species and no clouds, we fixed this parameter and used the highest VMR available for each species for the entire analysis. In particular, VMR = 10^{-1} for H_2O and CO, VMR = 10^{-2} for CH_4, NCH and NH_3, VMR = 10^{-3} for C_2H_2 and CO_2. The detection significance is calculated through a Welch t-test (Welch 1947), which consists of creating two distributions of cross-correlation values, one in trail within ±3 km s^{-1} around the expected planet's RV, and one out of trail considering the values ±25 km s^{-1} away from the planet's RV. The null hypothesis is when the two samples

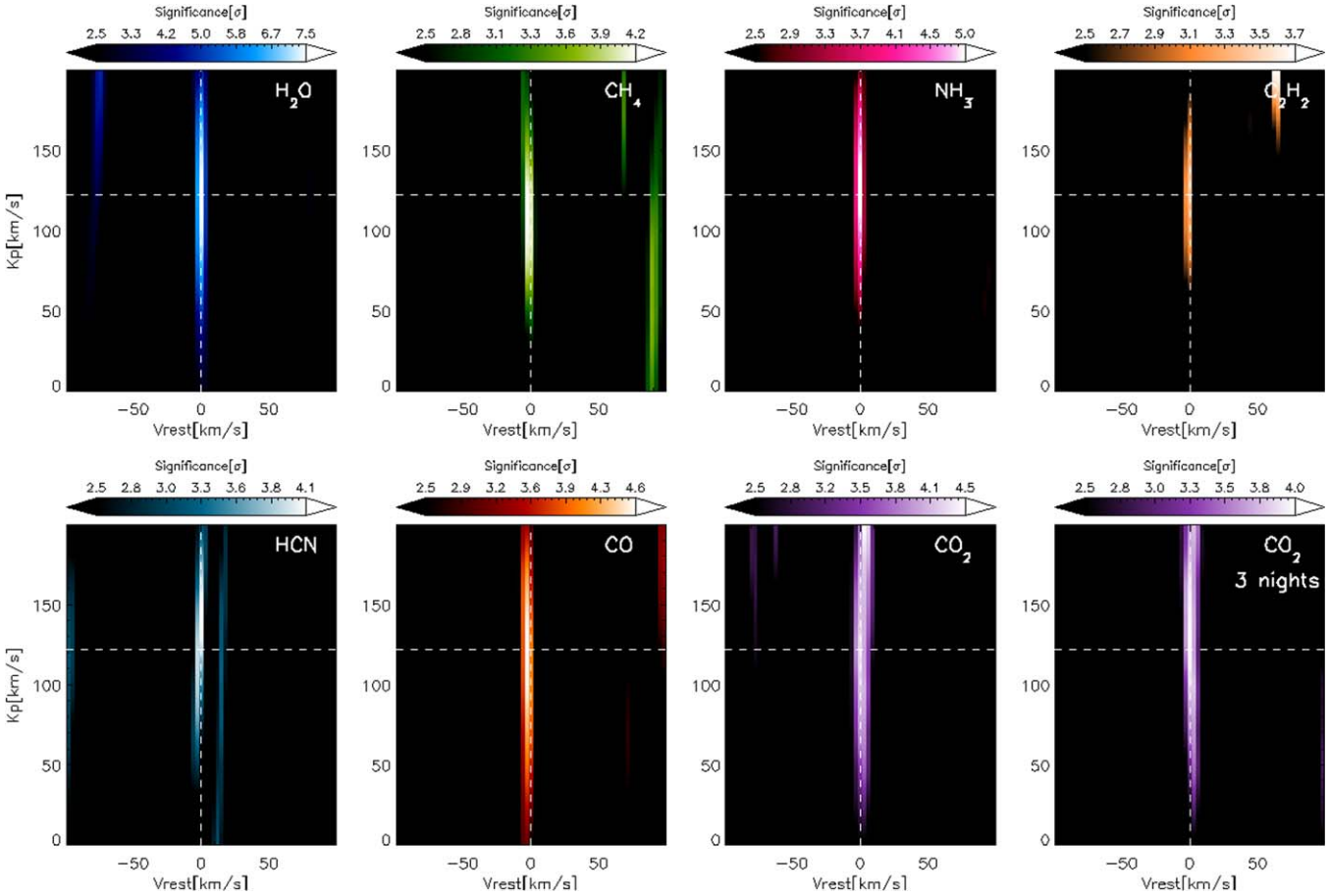

Figure 1. Significance maps of the cross correlation between the GIANO-B spectra and the isothermal atmospheric models, as a function of the planet's maximum radial velocity (K_P) and the planet's rest-frame velocity (v_{rest}). For a better visualization, the maps do not show any signal $<2.5\sigma$. The dashed white lines indicate the known velocity for WASP-80 b ($K_P = 122$ km s^{-1}, $v_{rest} = 0$ km s^{-1}). The CO_2 map is also shown in the case of coadding only the three nights (not including the third night). See discussion in the text (Section 3) and Table 2.

have the same mean. The rejection of the null hypothesis represents the significance of the detection. We claim a detection if $\sigma \geqslant 4$.

From the CC analysis, we detect five out of seven tested species, namely H_2O (7.5σ), CH_4 (4.2σ), NH_3 (5σ), HCN (4.1σ), and CO (4.6σ). The results are displayed in Table 2 and the significance maps as a function of the rest-frame velocity v_{rest} and the planetary semiamplitude K_P are shown in Figure 1. We find a tentative evidence for C_2H_2, since the most significant peak in the map is located at $v_{rest} = 63$ km s^{-1} with 3.7σ, but the second significant peak is at the planetary position with a slightly lower $\sigma = 3.4$. As for CO_2, the most significant peak (4.45σ) is at the upper limit of the K_P range, even though a signal at the nominal (K_P, v_{rest}) position is visible, though at a slightly lower significance (4.28σ) than the main peak. Since CO_2 can be strongly affected by the tellurics and, during the third night (2020 June 26) the tellurics position falls close to $v_{rest} = 0$, we performed the analysis for CO_2 not including this night, and we found a 4.01σ detection at the planetary position (see Table 2), confirming that the result might be affected by telluric contamination.

The H_2O signal is so strong that we can detect it in each night separately. Conversely, the rest of the detected molecules have weaker signals and are not always detected in each single transit, but are solidly detected by coadding the four transits. These results demonstrate the advantage of the multitransit strategy when searching for molecular species in planetary atmospheres.

Likelihood analysis—after performing the cross-correlation approach, we convert the CCFs into likelihood (LH) values (Brogi & Line 2019). Briefly, the log-likelihood function is defined as in Equation (9) of Brogi & Line (2019):

$$\log L = -\frac{N}{2}\log[s_f^2 - 2R(s) + s_g^2], \quad (1)$$

where N is the number of spectral channels, s_f^2 is the variance of the data, s_g^2 the variance of the model, and $R(s)$ the cross covariance between the data and the model with s being a bin/wavelength shift. This function is computed for each order and each spectrum. The final log-likelihood value is the sum of all log-likelihood functions for each night. As in Giacobbe et al. (2021), an additional free parameter, namely the line-intensity scaling factor S, is introduced in this framework. If the model (i.e., the strength of the spectral lines) perfectly matches the data, S will be 1, which means $\log S = 0$. Unlike in the CC (which is a normalized quantity), the line depth is important in the LH framework and the scaling factor allows us to approximate the continuum of the model as well as to take into account the effects from other species. In this framework, we calculate the significance by comparing the maximum value

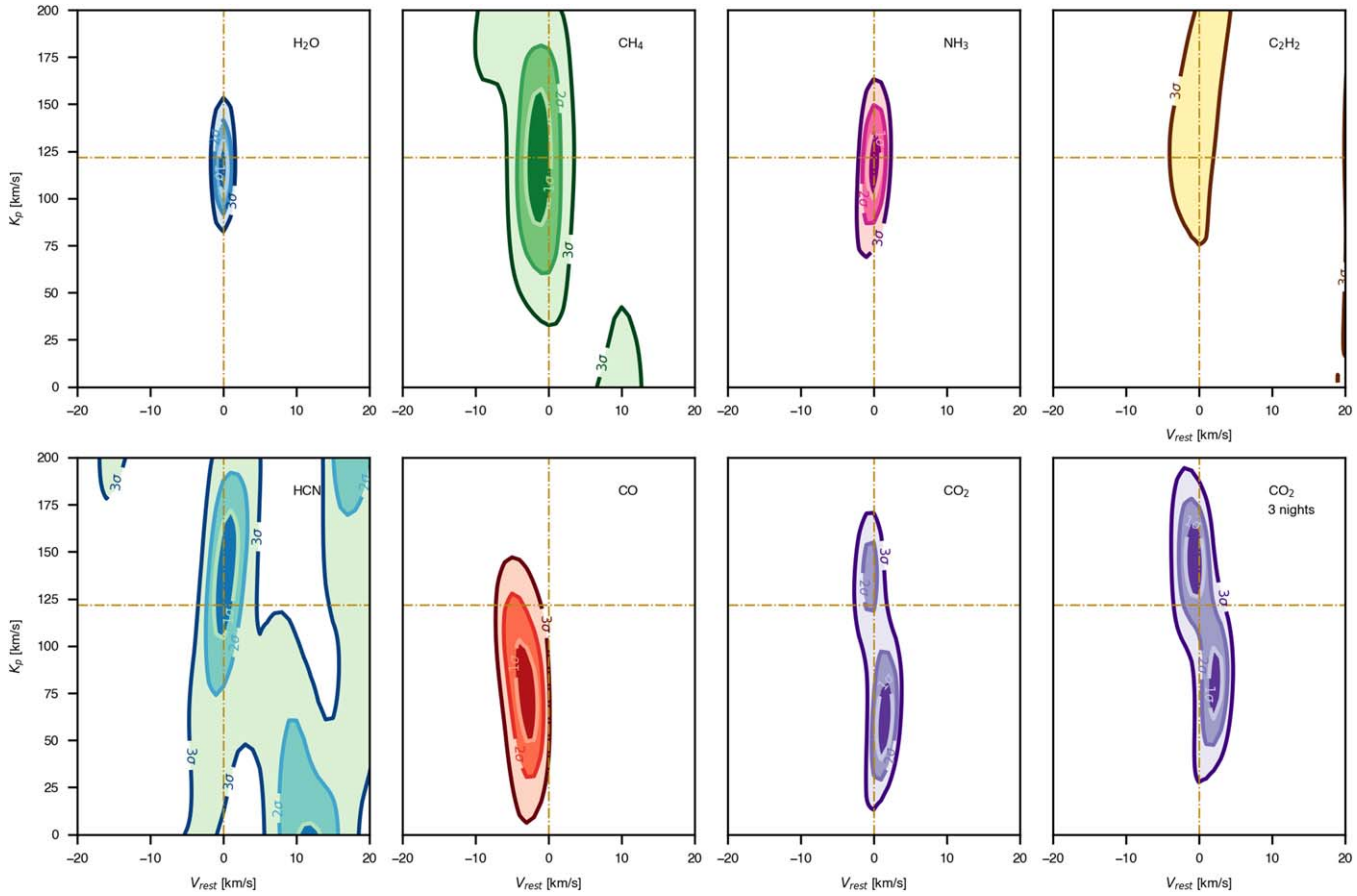

Figure 2. Likelihood confidence intervals maps for each investigated molecule as a function of K_P and v_{rest} and at the best-fit scaling factor. The dashed lines represent the nominal planetary velocities. As for the CC significance maps, the CO_2 likelihood map is displayed in the case of coadding only three nights (not including the third night). As regards C_2H_2, the likelihood intervals map does not significantly change by coadding three or four nights.

of the likelihood to the mean LH value in the map used as baseline.

The likelihood function is computed for each order, each observed spectrum and each night on a grid of K_P ([0, 200] km s^{-1} in steps of 1 km s^{-1}), v_{rest} ([−99, 99] km s^{-1} in steps of 1 km s^{-1}), and $\log S$ ([−1.1, 1.1] in steps of 0.1). Table 2 reports the v_{rest}, K_P and $\log S$ values, while Figure 2 shows the log-likelihood confidence interval maps for each molecule maximized at the best-fit scaling factor for the model, with a zoomed v_{rest} interval between [−20, 20] km s^{-1} for a better readability. The original version of this map is shown in Figure 4 in Appendix B. Since in our analysis we used fixed VMRs and single-species model (meaning that the line contrast is deeper than in a mixed model), the log S values are only indicative and cannot be properly interpreted.

In this likelihood framework, we confirm four out of five molecules detected with the CC, namely H_2O, CH_4, NH_3, and HCN. As in the case of the CC approach, CO_2 is not detected in the four-night case, showing a significant peak at low K_P values, even though a slightly less significant peak (4.28σ) is present in the likelihood map as well. Furthermore, when we exclude the third night, the peak around the planetary K_P becomes the most significant in the map (see Figure 2).

Finally, the CO signal shows a low value of K_P in the likelihood map, which is not compatible with the nominal K_P (see Figure 2). This low value can be due to the contamination of the stellar CO lines, which is quasistationary in wavelength. In fact, because of its rotation, the stellar absorption lines are distorted by the Rossiter–McLaughlin (RM) effect and, during the transit, this effect can cause spurious signals at different transit phases, and finally in the detection maps, being of the same order of magnitude of the planetary signal. Unlike other molecules, the RM effect can heavily affect the CO detection (Brogi et al. 2016). In order to investigate this contamination, we first calculate the theoretical expected K_P for the stellar atmosphere as $v \sin i / \sin(2\pi\phi_1)$, where ϕ_1 is the phase at transit ingress (0.014 for WASP-80). We find that the expected K_P corresponding to the stellar CO is 40.4 km s^{-1}, which is lower than the K_P value for the LH peak. On the other hand, it is possible that our LH result might be a combination of the stellar and planetary signal, which would appear at intermediate K_P values. As an additional test, we generated a synthetic stellar spectrum with the effective temperature, $\log g_*$, and metallicity values of WASP-80, from the PHOENIX spectral library (Husser et al. 2013). We convolved this spectrum to the GIANO-B resolution and calculated the CCFs and the LH using the PHOENIX spectrum to mask the stellar lines in our observed spectra. This operation did not improve the previous results, thus resulting inconclusive.

The difference between the CC and LH maps reflects the fact that, while the CC analysis is mostly sensitive to the line position and relative (i.e., line-to-line) amplitude, the LH analysis is additionally sensitive to the line shape and the line-to-wing contrast ratio. Therefore, a model that matches well the line position in CC might still be penalized in the LH analysis if the line shape/amplitude is mismatched. This is also a strong

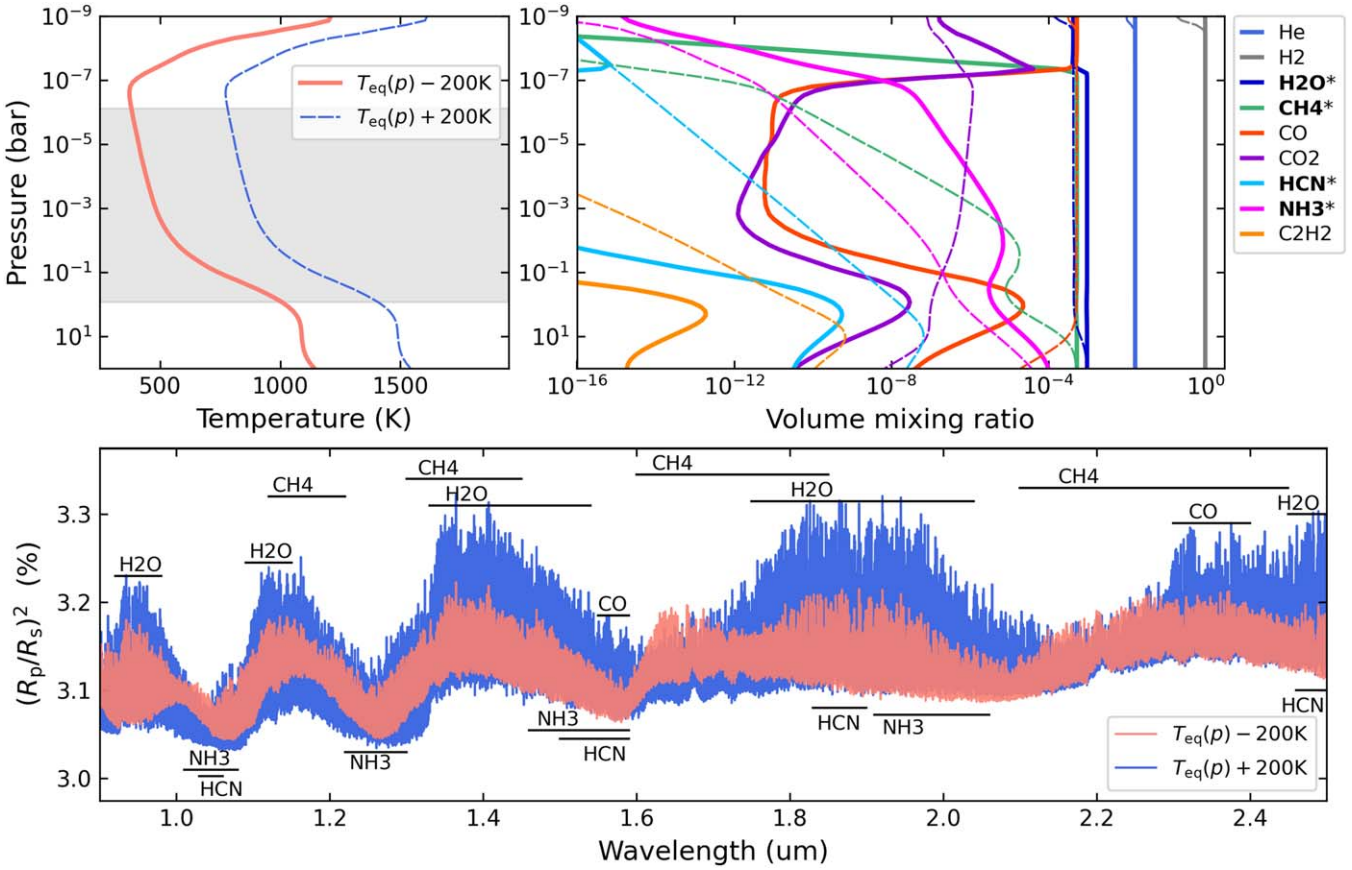

Figure 3. Sample atmospheric models for WASP-80 b in radiative and thermochemical equilibrium for a solar elemental composition. The top-left panel shows the equilibrium temperature profile shifted by ±200 K, to simulate a low-temperature case (thick solid red line) and a high-temperature case (thin dashed blue line). The shaded area denotes the pressure range probed by the GIANO-B transmission observations for these models. The top-right panel shows the equilibrium composition for the two temperature profiles at low (thick solid lines) and high temperature (thin dashed lines), color coded for each relevant species (see legend, with the asterisks indicating the firmly detected species). The bottom panel shows the transmission spectra over the GIANO-B wavelength range, for the low-temperature case (red) and high-temperature model (blue). The horizontal black lines denote the wavelength ranges where each of the labeled species are expected to significantly shape the transmission spectrum of WASP-80 b.

motivation for presenting both the CC and LH analyses even in the absence of a full atmospheric retrieval. While the LH is advantageous in the amount of information extracted from the spectra, it is also more demanding in terms of the accuracy of the modeling. On the other hand, the CC analysis is probably better at detecting species even with imperfect templates, which is valuable at the exploratory stage.

4. Atmospheric Modeling

Given the rich set of molecular detections by GIANO-B on WASP-80 b, we can make rough estimates of the physical properties of the planet being guided by the observations, even without quantitative abundance estimates. In fact, WASP-80 b sits at a particularly favorably location in the parameter space to probe its temperature profile because its equilibrium temperature straddles between two regimes where either CO ($T > T_{eq}$) or CH_4 ($T < T_{eq}$) dominate the carbon chemistry (e.g., Moses et al. 2013), thus making the composition particularly sensitive to the temperature profile. We therefore adopted the temperature as a main parameter to focus our exploration.

To model the atmospheric properties and theoretical spectra of WASP-80 b, we used the Pyrat Bay[23] open-source modeling framework (Cubillos & Blecic 2021), We explored potential physical scenarios under radiative and thermochemical equilibrium (see details in Appendix A), parameterized by the planet's metallicity and C/O elemental ratio. Certainly, given the equilibrium temperature of WASP-80 b, processes like photochemistry or transport-induced quenching can drive the atmosphere out of chemical equilibrium (Moses 2014). Thus, we consider the qualitative effects of disequilibrium chemistry on our models as well.

Figure 3 shows two examples of WASP-80 b models for a solar metallicity and C/O ratio, where we have shifted the equilibrium temperature profile by ±200 K, and recomputed the thermochemical equilibrium abundances and their respective transmission spectra. The variation in temperature has a significant impact in both the composition and the transmission spectra.

For the higher-temperature model CO dominates the carbon chemistry, with H_2O capturing the remaining—still largely available—oxygen (thin dashed lines). CH_4 is abundant in deeper layers, steadily decreasing with altitude. In contrast, for the lower-temperature model CH_4 dominates the carbon chemistry (solid thick lines), H_2O dominates then the oxygen chemistry, which leads to a much diminished CO abundance. Spectroscopically, both H_2O and CH_4 should present detectable absorption features in both models (having both broad absorption bands across the 0.9–2.5 μm spectrum), although

[23] https://github.com/pcubillos/pyratbay

the spectra are mainly shaped by H_2O bands at high temperatures and CH_4 at low temperatures, due to the different relative abundances between these molecules (see bottom panel of Figure 3).

The CO molecule, in contrast, only presents strong absorption in narrow bands (1.6 and 2.5 μm) and should only be detectable in the spectrum of the higher-temperature model. A conclusive detection of CO would have favored the higher-temperature scenario, but this is not the case. The chain of reactions in the chemical network leads to drastic changes in the abundances for most other trace species as well, with CO_2, HCN, and C_2 being more abundant in the higher-temperature case by several orders of magnitude. The abundance of NH_3 is somewhat decoupled from the carbon and oxygen chemistry, being more abundant at lower temperatures. At their equilibrium abundances, neither NH_3 nor HCN would present detectable features in the transmission spectra in both the low- and high-temperature models.

The detection of NH_3 and HCN would thus require to invoke disequilibrium chemistry processes that enhanced their abundances. Specifically, transport-induced quenching can drive the deep-interior abundance throughout the atmosphere, with NH_3 and CH_4 being two major species expected to be quenched. The HCN abundance can be further enhanced by a pseudo equilibrium with the quenched CH_4 and NH_3 and be produced photochemically by stellar ultraviolet photons (see Moses 2014 and references therein). With this in mind, both modeled cases would show evidence of NH_3 absorption when quenched from the lower layers. However, HCN would only be detectable on the higher-temperature case since its abundance at depth (from where it would be quenched) is $\sim$2 orders of magnitude larger than in the low-temperature case. Thus, the detection of HCN also points toward the higher-temperature case.

Finally, we also explored nonsolar compositions. In terms of the global metallicity, CO_2 is the molecule most strongly enhanced with increasing metallicity, becoming detectable at metallicities greater than $\sim 10\times$ solar. Thus, a confirmation of the tentative detection of CO_2 would point toward supersolar metallicities in the atmosphere of WASP-80 b. Our results for subsolar metallicity runs ($0.1\times$) are qualitatively similar to our solar ones. In terms of C/O ratios we also considered carbon-rich atmospheres, due to the strong impact on the chemistry (e.g., Madhusudhan et al. 2011; Madhusudhan 2012; Moses et al. 2013). We found that elemental ratios of $C/O > 1$ are discouraged since the H_2O abundance decreases, favoring then hydrocarbon species like CH_4, HCN, or C_2.

The qualitative picture emerging from the comparison of the detected molecules with the atmospheric models we run provides tentative indications on WASP-80b's formation history. The metallicity of the host star WASP-80 is subsolar (Triaud et al. 2013), whereas our observations suggest a subsolar-to-solar planetary metallicity. Within this range of possibilities, if the planet had a superstellar metallicity, combined with the solar C/O ratio estimation for WASP-80b, our observations would favor formation scenarios where the giant planet accreted a significant mass of planetesimals while migrating through its native circumstellar disk (Turrini et al. 2021, 2022, Pacetti et al. 2022). While the current data do not allow to draw stronger conclusions (e.g., on the extent of WASP-80b's migration), our NH3 detection makes WASP-80b a prime target for future efforts to quantify the abundances of C, O, and N in its atmosphere and use their ratios to probe its formation history in more details (Kolecki & Wang 2021; Turrini et al. 2021, 2022; Biazzo et al. 2022; Pacetti et al. 2022). In particular, the present work will complement and help in the interpretation of JWST spectra of WASP-80 b whose transit and eclipse observations are planned through the GTO programs (PIDs 1177, 1185, and 1201).

5. Conclusions and Future Perspectives

We report on the detection of multiple molecular species in the atmosphere of the warm Jupiter, WASP-80 b, by analyzing nIR transmission spectra gathered with GIANO-B at TNG during four transits. We used two different statistical frameworks: the cross-correlation function technique and the likelihood approach. We summarize the detections as follows: we report significant detections for H_2O, CH_4, NH_3, and HCN, tentative detection for CO_2. We have inconclusive results for C_2H_2 and CO, whose presence in the WASP-80 b atmosphere cannot be either firmly confirmed or excluded (see discussion in Section 3), but more observations and higher S/N data will help disentangling the nature of the signals (Figures 1 and 2).

The statistically robust detection of several species on WASP-80 b paves the way to estimate the chemical and physical conditions of the planet's atmosphere. Our initial exploration considering radiative-thermochemical equilibrium models and the impact of disequilibrium processes suggest that the atmosphere is compatible with a solar composition (H_2O and CH_4 detections), possibly affected by disequilibrium chemistry (NH_3 and HCN detections). Future confirmation of the detection (or nondetection) of CO will place strong constraints on the temperature profile. Likewise, a confirmation of CO_2 will help to constrain the atmospheric metallicity.

These results demonstrate for the first time that not only hot Jupiters (Giacobbe et al. 2021), but also warm giant planets present a rich chemistry in their atmosphere, breaking new ground in the study of exoplanetary atmospheres. With recent (e.g., CRIRES+ and JWST) and future upcoming (e.g., ELTs and ARIEL) instruments, it will be possible to combine multiple wavelength bands and resolutions to derive accurate and precise molecular abundances as well as atmospheric elemental ratios (e.g., the C/O, N/O, and C/N ratios) and metallicity, thus confirming/updating our qualitative estimates of solar C/O and metallicity under the assumption of thermochemical equilibrium, and our tentative constraints on WASP-80 b's formation history. In particular, the combined information provided by the abundance ratios of elements with different volatility, like C, O, and N revealed by our detections in WASP-80b's atmosphere, provides a direct window into the formation and migration history of giant planets (Kolecki & Wang 2021; Turrini et al. 2021, 2022). The improved estimates of the abundance of these elements achievable by such future facilities will therefore allow us to reconstruct the details of WASP-80b's formation history.

We acknowledge financial contributions from PRIN INAF 2019 and from the agreement ASI-INAF number 2018-16-HH. P. C. was funded by the Austrian Science Fund (FWF) Erwin Schroedinger Fellowship J4595-N. M.B. ackowledges support from from the UK Science and Technology Facilities Council (STFC) research grant ST/T000406/1. D.T. and E.S. acknowledge the support of the Italian National Institute of Astrophysics (INAF) through the INAF Main Stream project "Ariel and the astrochemical link between circumstellar disks and

planets" (CUP: C54I19000700005) and ASI-INAF contract no. 2021-5-HH.0. VNa, IPa, GPi, and GSc acknowledge support from CHEOPS ASI-INAF agreement n. 2019-29-HH.0.

Software: PYRAT BAY (Cubillos & Blecic 2021), REPACK (Cubillos 2017), TEA (Blecic et al. 2016), NUMPY (Harris et al. 2020), SCIPY (Virtanen et al. 2020), SYMPY (Meurer et al. 2017), MATPLOTLIB (Hunter 2007), IPYTHON (Pérez & Granger 2007), and BIBMANAGER (Cubillos 2019).

Facilities: TNG(GIANO-B).

Appendix A
Radiative-equilibrium Modeling

To setup the PYRAT BAY modeling framework to attain radiative and thermochemical equilibrium, we solved the radiative-transfer equation in an iterative approach, under the two-stream, plane-parallel, local-thermodynamic, and hydrostatic approximations (following Heng et al. 2014; Malik et al. 2017). To enforce chemical equilibrium, we calculated the compositions using the thermochemical-equilibrium abundances code TEA (Blecic et al. 2016) for input elemental composition, temperature, and pressure profiles. In this work we modeled a chemical network containing H, He, C, N, O, Na, K, H_2, H_2O, CH_4, CO, CO_2, OH, C_2, C_2H_4, N_2, NH_3, and HCN. Simultaneously, to enforce radiative equilibrium the code updates the temperature profile until the divergence of the upward–downward net fluxes converges to a negligible value at each layer. As boundary conditions we imposed a 100 K blackbody internal radiative heat and an incident stellar irradiation according to the properties of WASP-80, assuming zero Bond albedo and full day–night energy redistribution.

We performed the radiative-transfer calculation over a fixed pressure profile ranging from 100 to 10^{-9} bar, and a wavelength grid ranging from 0.3 to 30 μm sampled with a 0.3 cm^{-1} spacing, sufficient to encompass the bulk of the stellar and planetary radiation (mainly in the optical and infrared, respectively). The radiative-transfer opacities include line lists for the most relevant molecular species, i.e., CO, CO_2, and CH_4 from HITEMP (Rothman et al. 2010; Li et al. 2015; Hargreaves et al. 2020); and of H_2O, HCN, NH_3, and C_2 from ExoMol Polyansky et al. (2018), Chubb et al. (2020), Yurchenko et al. (2011), Harris et al. (2006, 2008), and Coles et al. (2019). To handle the billion-sized ExoMol line lists, we employed the REPACK algorithm (Cubillos 2017) to extract only the dominant transitions, reducing the number of transitions by a factor of ~100 without a significant impact on the resulting opacities. In addition to the molecular opacities, the PYRAT BAY code included alkali resonance-line opacities for Na and K (Burrows et al. 2000): Rayleigh opacity for H, H_2, and He (Kurucz 1970); and collision-induced absorption for H_2–H_2 and H_2–He (Borysow et al. 2001; Borysow 2002; Richard et al. 2012).

Appendix B
Likelihood maps

Figure 4 shows the log-likelihood confidence interval maps for each molecule maximized at the best-fit scaling factor for the model, with a v_{rest} interval between [−99, 99] km s^{-1}.

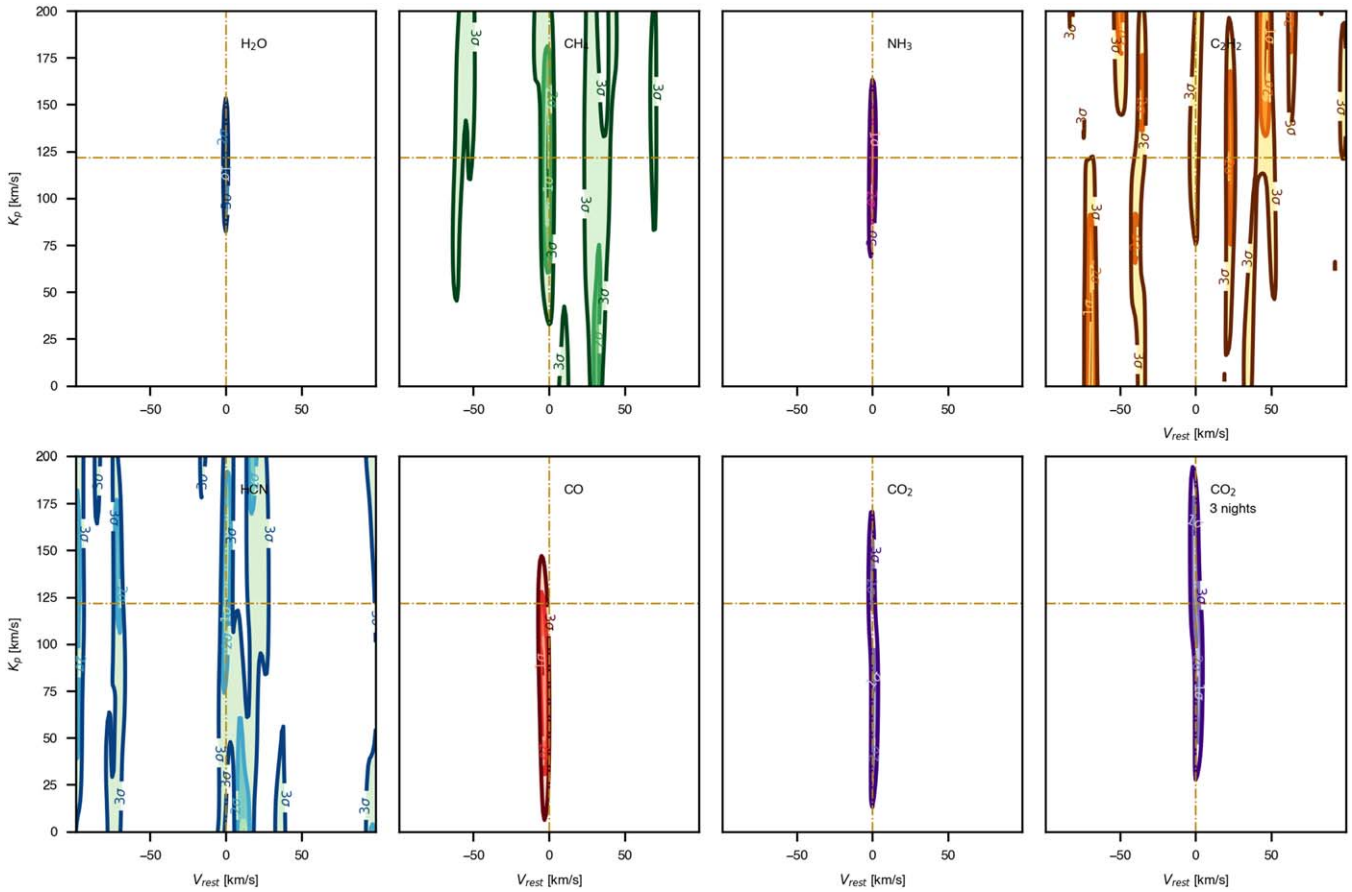

Figure 4. As Figure 2 but with v_{rest} interval between [−99, 99] km s^{-1}.

ORCID iDs

Ilaria Carleo https://orcid.org/0000-0002-0810-3747
Paolo Giacobbe https://orcid.org/0000-0001-7034-7024
Gloria Guilluy https://orcid.org/0000-0002-1259-2678
Patricio E. Cubillos https://orcid.org/0000-0002-1347-2600
Aldo S. Bonomo https://orcid.org/0000-0002-6177-198X
Alessandro Sozzetti https://orcid.org/0000-0002-7504-365X
Matteo Brogi https://orcid.org/0000-0002-7704-0153
Siddharth Gandhi https://orcid.org/0000-0001-9552-3709
Luca Fossati https://orcid.org/0000-0003-4426-9530
Diego Turrini https://orcid.org/0000-0002-1923-7740
Katia Biazzo https://orcid.org/0000-0002-1892-2180
Francesco Borsa https://orcid.org/0000-0003-4830-0590
Antonino F. Lanza https://orcid.org/0000-0001-5928-7251
Luca Malavolta https://orcid.org/0000-0002-6492-2085
Antonio Maggio https://orcid.org/0000-0001-5154-6108
Luigi Mancini https://orcid.org/0000-0002-9428-8732
Lorenzo Pino https://orcid.org/0000-0002-1321-8856
Ennio Poretti https://orcid.org/0000-0003-1200-0473
Monica Rainer https://orcid.org/0000-0002-8786-2572
Gaetano Scandariato https://orcid.org/0000-0003-2029-0626
Eugenio Schisano https://orcid.org/0000-0003-1560-3958
Gloria Andreuzzi https://orcid.org/0000-0001-5125-6397
Andrea Bignamini https://orcid.org/0000-0002-5606-6354
Rosario Cosentino https://orcid.org/0000-0003-1784-1431
Aldo Fiorenzano https://orcid.org/0000-0002-4272-4272
Emilio Molinari https://orcid.org/0000-0002-1742-7735
Marco Pedani https://orcid.org/0000-0002-5752-6260
Seth Redfield https://orcid.org/0000-0003-3786-3486

References

Barbato, D., Pinamonti, M., Sozzetti, A., et al. 2020, A&A, 641, A68
Barber, R. J., Strange, J. K., Hill, C., et al. 2014, MNRAS, 437, 1828
Biazzo, K., D'Orazi, V., Desidera, S., et al. 2022, arXiv:2205.15796
Birkby, J. L. 2018, arXiv:1806.04617
Blecic, J., Harrington, J., & Bowman, M. O. 2016, ApJS, 225, 4
Bonomo, A. S., Desidera, S., Benatti, S., et al. 2017, A&A, 602, A107
Borsa, F., Rainer, M., Bonomo, A. S., et al. 2019, A&A, 631, A34
Borysow, A. 2002, A&A, 390, 779
Borysow, A., Jorgensen, U. G., & Fu, Y. 2001, JQSRT, 68, 235
Brogi, M., de Kok, R. J., Albrecht, S., et al. 2016, ApJ, 817, 106
Brogi, M., & Line, M. R. 2019, AJ, 157, 114
Burrows, A., Marley, M. S., & Sharp, C. M. 2000, ApJ, 531, 438
Carleo, I., Benatti, S., Lanza, A. F., et al. 2018, A&A, 613, A50
Carleo, I., Malavolta, L., Lanza, A. F., et al. 2020, A&A, 638, A5
Chubb, K. L., Tennyson, J., & Yurchenko, S. N. 2020, MNRAS, 493, 1531
Claudi, R., Benatti, S., Carleo, I., et al. 2017, EPJP, 132, 364
Coles, P. A., Yurchenko, S. N., & Tennyson, J. 2019, MNRAS, 490, 4638
Cosentino, R., Lovis, C., Pepe, F., et al. 2012, Proc. SPIE, 8446, 84461V
Cosentino, R., Lovis, C., Pepe, F., et al. 2014, Proc. SPIE, 9147, 91478C
Cubillos, P. E. 2017, ApJ, 850, 32
Cubillos, P. E. 2019, bibmanager: A BibTeX manager for LaTeX projects, Zenodo, doi:10.5281/zenodo.2547042
Cubillos, P. E., & Blecic, J. 2021, MNRAS, 505, 2675
Damasso, M., Lanza, A. F., Benatti, S., et al. 2020, A&A, 642, A133
Fisher, C., & Heng, K. 2018, MNRAS, 481, 4698
Fossati, L., Guilluy, G., Shaikhislamov, I. F., et al. 2022, A&A, 658, A136
Gandhi, S., & Madhusudhan, N. 2017, MNRAS, 472, 2334
Gandhi, S., Brogi, M., Yurchenko, S. N., et al. 2020, MNRAS, 495, 224
Giacobbe, P., Brogi, M., Gandhi, S., et al. 2021, Natur, 592, 205
Guilluy, G., Andretta, V., Borsa, F., et al. 2020, A&A, 639, A49
Guilluy, G., Giacobbe, P., Carleo, I., et al. 2022, arXiv:2207.09760
Hargreaves, R. J., Gordon, I. E., Rey, M., et al. 2020, ApJS, 247, 55
Harris, C. R., Millman, K. J., van der Walt, S. J., et al. 2020, Natur, 585, 357
Harris, G. J., Larner, F. C., Tennyson, J., et al. 2008, MNRAS, 390, 143
Harris, G. J., Tennyson, J., Kaminsky, B. M., Pavlenko, Y. V., & Jones, H. R. A. 2006, MNRAs, 367, 400
Heng, K., Mendonça, J. M., & Lee, J.-M. 2014, ApJS, 215, 4
Hood, C. E., Fortney, J. J., Line, M. R., et al. 2020, AJ, 160, 198
Huang, X., Freedman, R. S., Tashkun, S. A., Schwenke, D. W., & Lee, T. J. 2013, JQSRT, 130, 134
Huang, X., Schwenke, D. W., Freedman, R. S., & Lee, T. J. 2017, JQSRT, 203, 224
Hunter, J. D. 2007, CSE, 9, 90
Husser, T. O., Wende-von Berg, S., Dreizler, S., et al. 2013, A&A, 553, A6
Kirk, J., Wheatley, P. J., Louden, T., et al. 2018, MNRAS, 474, 876
Kolecki, J. R., & Wang, J. 2021, arXiv:2112.02031
Kurucz, R. L. 1970, SAO Special Report #309
Li, G., Gordon, I. E., Rothman, L. S., et al. 2015, ApJS, 216, 15
López-Morales, M., & Seager, S. 2007, ApJL, 667, L191
Madhusudhan, N. 2012, ApJ, 758, 36
Madhusudhan, N. 2019, ARA&A, 57, 617
Madhusudhan, N., Harrington, J., Stevenson, K. B., et al. 2011, Natur, 469, 64
Malik, M., Grosheintz, L., Mendonça, J. M., et al. 2017, AJ, 153, 56
Mancini, L., Southworth, J., Ciceri, S., et al. 2014, A&A, 562, A126
Mansfield, M., Line, M. R., Bean, J. L., et al. 2021, NatAs, 5, 1224
Meurer, A., Smith, C. P., Paprocki, M., et al. 2017, PeerJ Comp. Sci., 3, e103
Moses, J. I. 2014, RSPTA, 372, 20130073
Moses, J. I., Madhusudhan, N., Visscher, C., & Freedman, R. S. 2013, ApJ, 763, 25
Oliva, E., Origlia, L., Baffa, C., et al. 2006, Proc. SPIE, 6269, 626919
Pacetti, E., Turrini, D., Schisano, E., et al. 2022, arXiv:2206.14685
Parviainen, H., Pallé, E., Chen, G., et al. 2018, A&A, 609, A33
Pérez, F., & Granger, B. E. 2007, CSE, 9, 21
Pino, L., Désert, J.-M., Brogi, M., et al. 2020, ApJL, 894, L27
Polyansky, O. L., Kyuberis, A. A., Zobov, N. F., et al. 2018, MNRAS, 480, 2597
Rainer, M., Harutyunyan, A., Carleo, I., et al. 2018, Proc. SPIE, 10702, 1070266
Richard, C., Gordon, I. E., Rothman, L. S., et al. 2012, JQSRT, 113, 1276
Rothman, L. S., Gordon, I. E., Barber, R. J., et al. 2010, JQSRT, 111, 2139
Sedaghati, E., Boffin, H. M. J., Delrez, L., et al. 2017, MNRAS, 468, 3123
Sing, D. K., Fortney, J. J., Nikolov, N., et al. 2016, Natur, 529, 59
Tennyson, J., Yurchenko, S. N., Al-Refaie, A. F., et al. 2016, JMoSp, 327, 73
Triaud, A. H. M. J., Anderson, D. R., Collier Cameron, A., et al. 2013, A&A, 551, A80
Triaud, A. H. M. J., Gillon, M., Ehrenreich, D., et al. 2015, MNRAS, 450, 2279
Tsiaras, A., Waldmann, I. P., Zingales, T., et al. 2018, AJ, 155, 156
Turrini, D., Schisano, E., Fonte, S., et al. 2021, ApJ, 909, 40
Turrini, D., Codella, C., Danielski, C., et al. 2022, ExA, 53, 225
Virtanen, P., Gommers, R., Oliphant, T. E., et al. 2020, NatMe, 17, 261
Welch, B. L. 1947, Biometrika, 34, 28
Yurchenko, S. N., Barber, R. J., & Tennyson, J. 2011, MNRAS, 413, 1828